2018

Melanocortin 1 receptor targeted imaging of melanoma with gold nanocages and positron emission tomography

Yongfeng Zhao
Washington University School of Medicine in St. Louis

Bo Pang
Georgia Institute of Technology

Lisa Detering
Washington University School of Medicine in St. Louis

Hannah Luehmann
Washington University School of Medicine in St. Louis

Miaoxin Yang
Georgia Institute of Technology

See next page for additional authors

Follow this and additional works at: https://digitalcommons.wustl.edu/open_access_pubs

Recommended Citation

Zhao, Yongfeng; Pang, Bo; Detering, Lisa; Luehmann, Hannah; Yang, Miaoxin; Black, Kvar; Sultan, Deborah; Xia, Younan; and Liu, Yongjian ,"Melanocortin 1 receptor targeted imaging of melanoma with gold nanocages and positron emission tomography." Molecular Imaging.17,. 1-9. (2018).
https://digitalcommons.wustl.edu/open_access_pubs/6897

Authors

Yongfeng Zhao, Bo Pang, Lisa Detering, Hannah Luehmann, Miaoxin Yang, Kvar Black, Deborah Sultan, Younan Xia, and Yongjian Liu

Melanocortin 1 Receptor Targeted Imaging of Melanoma With Gold Nanocages and Positron Emission Tomography

Yongfeng Zhao, PhD[1,2], Bo Pang, PhD[3], Lisa Detering, MS[1],
Hannah Luehmann, MS[1], Miaoxin Yang, PhD[3], Kvar Black, PhD[1],
Deborah Sultan, BS[1], Younan Xia, PhD[3], and Yongjian Liu, PhD[1]

Abstract

Purpose: Melanoma is a lethal skin cancer with unmet clinical needs for targeted imaging and therapy. Nanoscale materials conjugated with targeting components have shown great potential to improve tumor delivery efficiency while minimizing undesirable side effects in vivo. Herein, we proposed to develop targeted nanoparticles for melanoma theranostics.

Method: In this work, gold nanocages (AuNCs) were conjugated with α-melanocyte-stimulating hormone (α-MSH) peptide and radiolabeled with ^{64}Cu for melanocortin 1 receptor-(MC1R) targeted positron emission tomography (PET) in a mouse B16/F10 melanoma model.

Results: Their controlled synthesis and surface chemistry enabled well-defined structure and radiolabeling efficiency. In vivo pharmacokinetic evaluation demonstrated comparable organ distribution between the targeted and nontargeted AuNCs. However, micro-PET/computed tomography (CT) imaging demonstrated specific and improved tumor accumulation via MC1R-mediated delivery. By increasing the coverage density of α-MSH peptide on AuNCs, the tumor delivery efficiency was improved.

Conclusion: The controlled synthesis, sensitive PET imaging, and optimal tumor targeting suggested the potential of targeted AuNCs for melanoma theranostics.

Keywords

gold nanocage, positron emission tomography, melanoma, melanocortin 1 receptor, α-melanocyte-stimulating hormone

Introduction

Skin cancer is the fifth most common cancer in the United States.[1] Of various dermatologic malignancies, melanoma accounts for only 1% of all the incidence but approximately 75% of the death in the case of skin cancer.[2] With the improvement in treatment strategies, malignant melanoma can be effectively treated upon early detection. However, the prognosis upon onset of metastasis is poor, as reflected by a 5-year survival rate of only 13% once distant malignancy has occurred.[3] Thus, early and sensitive detection of melanoma is of paramount importance in improving prognosis and patient survival. In addition, malignant melanoma is extraordinarily resistant to chemotherapy, immunotherapy, and external beam radiation therapy. Thus, new therapeutics are urgently needed for melanoma.

Nanoparticles, due to the size-promoted enhanced permeability and retention effect in leaky tumor vasculature, have been widely used for cancer imaging and therapy. Moreover, the high surface area to volume ratio of nanoparticles also enables the conjugation of targeting ligands, loading/encapsulation of therapeutic payloads, and labeling of diagnostic elements. Nanoparticles have been widely studied as multivalent platforms for cancer theranostics.[4-6] Of them, the gold

[1] Department of Radiology, Washington University School of Medicine, St. Louis, MO, USA
[2] Department of Chemistry and Biochemistry, Jackson State University, Jackson, MS, USA
[3] The Wallace H. Coulter Department of Biomedical Engineering, Georgia Institute of Technology and Emory University, Atlanta, GA, USA

Corresponding Author:
Yongjian Liu, Department of Radiology, Washington University School of Medicine, 510 S. Kingshighway Blvd, St. Louis, MO 63110 USA.
Email: yongjianliu@wustl.edu

nanoparticles with photothermal capability hold great promise as a theranostic platform for image-guided cancer therapy.[7-11] In our previous studies, we have examined the pharmacokinetics, tumor targeting, and intratumoral distribution of a variety of gold nanostructures with different sizes and shapes.[12-15] Gold nanocage (AuNCs), due to their efficient photothermal conversion and favorable biodistribution, are a unique type of nanostructure for targeted cancer nanomedicine.[12,13,15,16] Among the various targets assessed in melanoma detection, melanocortin 1 receptor (MC1R) has been widely studied due to its critical role in the incidence and progression of melanoma, making it a valid biomarker for the diagnosis of not only primary tumors but also metastasis in distant organs.[17,18] By conjugating [Nle[4], D-Phe[7]]-α-melanocyte-stimulating hormone (NDP-α-MSH), Lu et al have demonstrated receptor-mediated active targeting and efficient photothermal ablation of melanoma with gold nanoshells in a murine tumor model.[19] However, the imaging potential of these targeted nanostructures for melanoma has not been fully realized as a reference to guide the treatment. Previously, we studied the photoacoustic imaging of melanoma using NDP-α-MSH-conjugated AuNCs (ca 60 nm in size) in a mouse B16 model showing sensitive and specific detection of tumors.[20] However, the pharmacokinetics and tumor targeting efficiency of AuNCs need further optimization to enhance its theranostic potential.

Herein, we prepared AuNCs of approximately 40 nm in size for MC1R-targeted imaging in a mouse B16/F10 melanoma model. Through ^{64}Cu radiolabeling, we examined the organ distribution profile of AuNCs and compared the tumor imaging efficiency of AuNCs conjugated with various amounts of NDP-α-MSH peptide.

Experimental

Chemicals and Reagents

Orthopyridyldisulfide-polyethylene glycol-N-hydroxysuccinimide (OPSS-PEG-SVA, MW $\approx$ 5000) and poly(ethylene glycol)monomethyl ether thiol (MW $\approx$ 5000) were both obtained from Laysan Bio (Arab, Alabama). S-2-(4-Aminobenzyl)-1,4,7,10-tetraazacyclododecane tetraacetic acid (NH$_2$-Bn-DOTA) was purchased from Macrocyclics (Dallas, Texas). [Nle[4], D-Phe[7]-Lys(Dde)]-α-MSH [NDP-MSH (Dde)-α-NH$_2$] peptide was customized by CPC Scientific (Sunnyvale, California). Other chemicals and reagents, including poly(vinylpyrrolidone) (PVP, MW $\approx$ 55 000), gold (III) chloride trihydrate (HAuCl$_4$.3H$_2$O), ascorbic acid, sodium chloride (NaCl), and phosphate-buffered saline (PBS) were obtained from Sigma-Aldrich (St. Louis, Missouri). All chemicals were used as received unless specified.

Synthesis of Gold Nanocages

Gold nanocages covered with PVP were prepared using a galvanic replacement reaction between Ag nanocubes and HAuCl$_4$ following a previously reported protocol.[21] The reaction was frequently monitored by measuring the localized surface plasmon resonance (LSPR) peaks with UV-Vis spectroscopy (Cary 50 spectrometer, Varian, Palo Alto, California) during the reaction. The reaction was stopped when the LSPR reached approximately 800 nm. After washing with saturated NaCl solution, the AuNCs were collected by centrifugation at 15 000×g for 15 minutes, and purified by washing with MilliQ water 3 times.
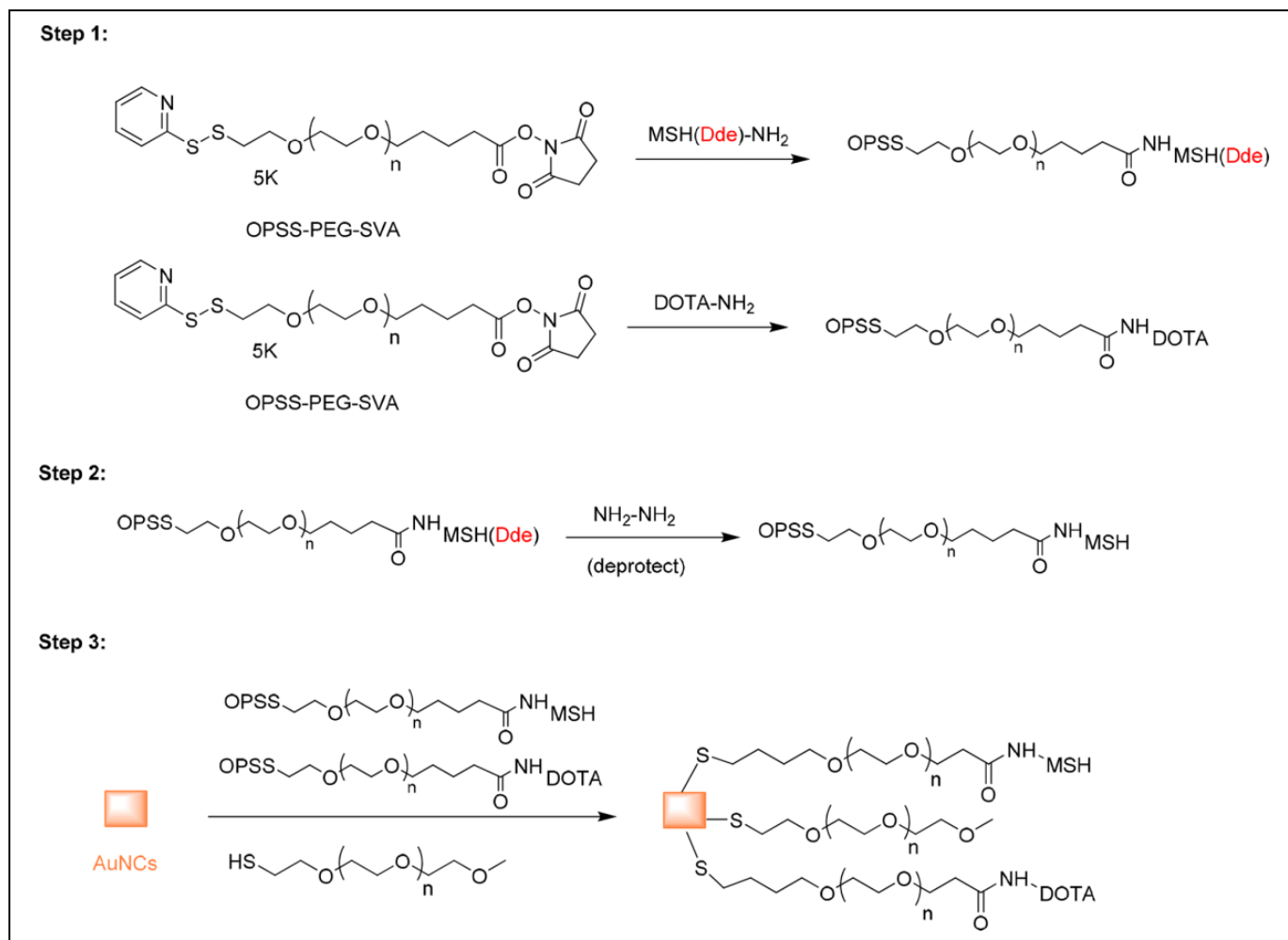
Preparation of OPPS-PEG-MSH

The OPSS-PEG-MSH molecule was prepared by coupling the primary amine group on the NDP-α-MSH peptide to OPSS-PEG-SVA (Figure 1). The amine-reactive OPSS-PEG-SVA was mixed with NDP-α-MSH (Dde)-NH$_2$ peptide in PBS (pH 7.4) at a molar ratio of 1:5 and allowed to react at 4°C overnight. The solution containing the OPSS-PEG-MSH(Dde) conjugate was desalted with a centrifuge filter (Amicon, 3 kDa) and washed with MilliQ water. The concentrated solution was recovered and lyophilized. The resulting solid was added to 2% hydrazine in N,N-dimethylformamide (DMF).[19] After 1 hour incubation at room temperature, the OPPS-PEG-MSH was precipitated by adding diethyl ether and collected by centrifugation at 22 000×g for 5 minutes. The supernatant was removed, and the remaining pellet was washed with diethyl ether. The pellet was further dried by air and stored at −20°C for future use.

Preparation of OPPS-PEG-DOTA

The OPSS-PEG-DOTA molecule was prepared by coupling the primary amine group on DOTA-NH$_2$ with OPSS-PEG-SVA. The amine-reactive OPSS-PEG-SVA was mixed with DOTA-NH$_2$ in pH 7.4 PBS buffer at a molar ratio of 1:5 and allowed to react at 4°C overnight. The solution containing the OPSS-PEG-DOTA was desalted with a centrifuge filter (Amicon, 3 kDa) and washed with MilliQ water.

Conjugation of PEG, PEG-DOTA, and PEG-MSH to AuNCs

The MSH peptide conjugated AuNCs (MSH-PEG-AuNCs) were prepared by adding AuNCs solution to a mixture of OPSS-PEG-MSH, OPPS-PEG-DOTA, and HS-PEG-OMe (MW $\approx$ 5000; OPSS-PEG-MSH:OPPS-PEG-DOTA:HS-PEG-OMe = 1:4:4) with a total PEG to AuNCs molar ratio of 10^5 to 1 (Figure 1). The mixture was allowed to incubate at 4°C overnight on a shaker. The conjugated AuNCs were purified by centrifugation at 11 000×g for 15 minutes. The pellet was redispersed in MilliQ water and centrifuged again. For AuNCs conjugated with a high density of MSH, the same conjugation strategy was used but with an elevated molar ratio of OPSS-PEG-MSH versus other PEG components (OPSS-PEG-MSH:OPPS-PEG-DOTA:HS-PEG-OMe = 1:1:1).

Figure 1. Scheme for the preparation of AuNC-PEG-MSH.

Comparison of Photothermal Effects of Nontargeted AuNCs-PEG and Targeted AuNCs-PEG-MSH

Aqueous suspensions of the nontargeted AuNCs-PEG and targeted AuNCs-PEG-MSH at identical concentrations were placed on a 96-well plate and irradiated with a diode laser ($\lambda = 808$ nm, Power Technology, Alexander, Arkansas) directly from above at a power density of 1.1 W/cm². The temperature changes were monitored using a NIR camera (ICI7320, Infrared Camera, Beaumont, Texas) placed on top of the suspension at 6-second intervals. The average temperature of the suspension was determined from the thermograph using IR Flash software (Infrared Camera, version 2.10) at each time point.

Radiolabeling of AuNCs-PEG-MSH and AuNCs-PEG

^{64}Cu ($t_{1/2} = 12.7$ h, $\beta^+ = 17\%$, $\beta^- = 40\%$) was produced on the Washington University Medical School CS-15 cyclotron by the ^{64}Ni (p, n) ^{64}Cu nuclear reaction. AuNCs-PEG-MSH or AuNCs-PEG (about 6 pmol) were incubated with 185 MBq ^{64}Cu^{2+} in 0.1 M ammonium acetate buffer (pH 5.5) at 45°C for 1 hour to achieve maximal labeling-specific activity. The

^{64}Cu-AuNCs-PEG-MSH or ^{64}Cu-AuNCs-PEG were dissolved in MilliQ water and purified by centrifugation at 15 000×*g* for 15 minutes followed by filtration through a 0.22 µmol/L syringe filter. After ethylenediaminetetraacetic acid (EDTA, 10 mmol/L in 50 mmol/L pH 7.4 phosphate buffer) challenge, the radiochemical purity of radiolabeled AuNCs was measured by radio instant thin layer chromatography (radio-iTLC, Bioscan, Washington, DC).

Biodistribution of ^{64}Cu-AuNCs-PEG-MSH or ^{64}Cu-AuNCs-PEG

All animal studies were performed in compliance with guidelines set forth by the NIH Office of Laboratory Animal Welfare and approved by the Washington University Animal Studies Committee. Biodistribution studies were performed in male C57BL/6 mice weighing 20 to 25 g (n = 4, Charles River Laboratory, Wilmington, Massachusetts) with 0.37 MBq (0.057 pmol) of ^{64}Cu-AuNCs-PEG-MSH or ^{64}Cu-AuNCs-PEG in 100 µL of saline (APP Pharmaceuticals, Schaumburg, Illinios) injected via the tail vein. The mice were anesthetized

with inhaled isoflurane during tracer injection and reanesthetized before euthanasia by cervical dislocation at each time point. Organs of interest were collected, weighed, and counted with a Beckman 8000 gamma counter (Beckman, Brea, California). Standards were prepared and measured along with the samples to calculate the percentage of the injected dose per gram of tissue (%ID/g).[10,22]

Positron Emission Tomography/Computed Tomography of ^{64}Cu-AuNCs-PEG-MSH

The B16/F10 cell line was obtained from the American Type Culture Collection (ATCC, Manassas, Virginia). The cells were cultured in Dulbecco's Modified Eagle's medium supplemented with 10% fetal bovine serum and 1% penicillin/streptomycin and incubated at 37°C in a humidified atmosphere of 5% CO_2. Ten days after 5×10^5 B16/F10 cells were implanted, nude mice were anesthetized with isoflurane and injected with 3.7 MBq (0.57 pmol) of ^{64}Cu-AuNCs-PEG-MSH in 100 μL of saline via the tail vein. MicroPET scans were performed on either microPET Focus 220 (Siemens, Malvern, Pennsylvania) or Inveon PET/CT system (Siemens) at 4, 24, and 48 hours postinjection. The competitive receptor blocking study was performed by coinjection of nonradiolabeled AuNCs-PEG-MSH and ^{64}Cu-AuNCs-PEG-MSH with a molar ratio of 35:1. The PET images were corrected for attenuation, scatter, normalization, and camera dead time and coregistered with CT images. Both PET scanners were cross-calibrated periodically. The PET images were reconstructed with the maximum a posteriori (MAP) algorithm and analyzed by ASIPro (Siemens Medical solutions, Knoxville, Tennessee). The tumor uptake of the radiolabeled AuNCs was calculated as %ID/g in 3-dimensional regions of interest.

Histology and Immunohistochemistry

Sections of tumor in 5 μm thickness were cut from paraformaldehyde-fixed (24 hours), paraffin-embedded specimens. The sections were deparaffinized and rehydrated through a series of xylenes and graded alcohols before undergoing antigen retrieval pretreatment (10 mmol/L Tris, 1 mmol/L EDTA, 0.05% Tween, pH 9.0, for 10 minutes). They were treated with 0.3% H_2O_2 for 30 minutes, followed by blocking serum for 1 hour to prevent nonspecific binding (Vectastain, Vector Laboratories, Burlingame, California). The sections were then incubated overnight at 4°C with primary antibody (anti-melanin, 1:100 in blocking serum, Santa Cruz Biotechnology, Dallas, Texas). Secondary antibody was applied (Vector Laboratories), and blue color development was achieved using an alkaline phosphatase-based immunostaining kit (Vector Laboratories).

Statistical Analysis

Group variation is described as the mean (standard deviation). Group comparisons were made using the student *t* test. The significance level in all tests was $P \leq .05$. GraphPad Prism v. 6.04 (La Jolla, California) was used for all statistical analyses.

Results and Discussion

Synthesis and Characterization of AuNCs-PEG-MSH

Previously, we used 50-nm AuNCs conjugated with [Nle[4], D-Phe[7]]-α-melanocyte-stimulating hormone (NDP-α-MSH) peptide for melanoma photoacoustic imaging and showed sensitive and specific detection of MC1R in a mouse B16 model.[20] However, the large size of AuNCs led to unfavorable in vivo pharmacokinetics and high uptake by the mononuclear phagocyte system (MPS: liver, and spleen). Thus, we prepared MC1R-targeted AuNCs-PEG-MSH using AuNCs with an edge length of 35 nm and a wall thickness of 3.6 nm (Figure 2A) by following the procedure outlined in Figure 1. Due to the well-defined structure and inherent optical properties of AuNCs, the surface modification did not change the LSPR peak of the AuNCs, which was illustrated by the almost identical LSPR peaks around 790 nm for the unmodified AuNCs, AuNCs-PEG, and AuNCs-PEG-MSH shown in Figure 2B.[20] Moreover, as shown in Figure 2C, the 3 samples of nanocages also displayed comparable efficiencies for the photothermal effect to convert light to heat, suggesting no aggregation during PEGylation.[19] Following our previous strategy for quantifying the PEGylation density,[13] the number of NDP-α-MSH peptides conjugated with the AuNCs was estimated to be approximately 1800 copies per AuNC. These nanocages were then efficiently radiolabeled with [64]Cu^{2+} through the DOTA chelator conjugated with the AuNCs, enabling high-specific activity (6.5 MBq/pmol) and trace amount (0.057 and 0.57 pmol for biodistribution and PET imaging, respectively) administration for in vivo applications. After centrifugal purification, the radiochemical purity of ^{64}Cu-AuNCs-PEG-MSH (> 95% pure) was confirmed by radio-iTLC (Figure 2D) prior to intravenous injection.

Biodistribution of AuNCs-PEG-MSH

Biodistribution studies of the purified ^{64}Cu-AuNCs-PEG-MSH and ^{64}Cu-AuNCs-PEG were conducted in wild-type C57BL/6 mice at 4 and 24 hours postinjection. As shown in Figure 3, the targeted and nontargeted nanocages showed comparable in vivo organ distribution profiles at the 2 time points. Both nanocages showed high blood retentions around 20% ID/g (20.30 ± 1.84%ID/g for ^{64}Cu-AuNCs-PEG and 19.89 ± 2.52%ID/g for ^{64}Cu-AuNCs-PEG-MSH) at 4 hours, followed by rapid decrease to less than 2%ID/g at 24 hours, which was also verified by the variations in other blood pool organs including heart and lungs. The high blood retention of both targeted and nontargeted nanocages indicates high efficiency of surface modification and is consistent with our previous study for nontargeted nanocages.[13] Although the uptake in MPS system was at least 2 times less than their bigger
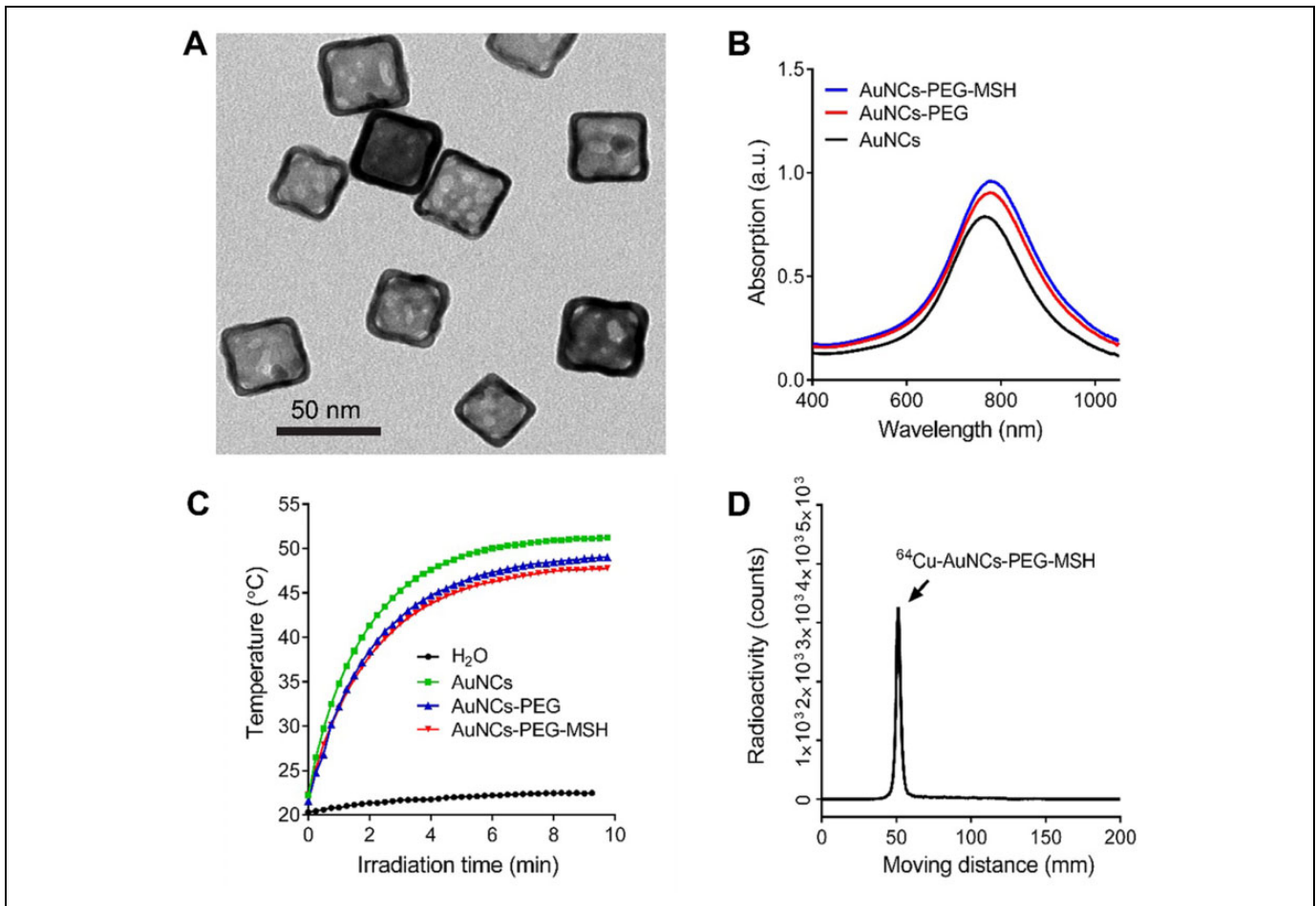
Figure 2. Characterization of gold nanocages. A, Transmission electron microscopy image of AuNC-PEG-MSH. B, UV-Vis spectra of unmodified gold nanocages (AuNCs), AuNCs-PEG, and AuNCs-PEG-MSH showing similar LSPR peaks. C, Plots of temperatures as a function of irradiation time for suspension of H_2O, AuNCs, AuNCs-PEG, AuNCs-PEG-MSH. The concentration (0.025 nmol/L) of each suspension had the same maximum extinction intensity. The laser power density was 1.1 W/cm³. D, Instant radio-thin layer chromatogram (iTLC) of purified ^{64}Cu-AuNCs-PEG-MSH.

counterpart,[13] due to the heavy metal nature and sizes,[23,24] both nanocages still had significant liver and spleen accumulation but slightly different patterns. In contrast to the slightly increased liver accumulations (12.4 ± 2.66%ID/g at 4 hours to 19.2 ± 0.91%ID/g at 24 hours) of ^{64}Cu-AuNCs-PEG, the hepatic uptake of ^{64}Cu-AuNCs-PEG-MSH was relatively stable during the 24-hour study (15.1 ± 3.92%ID/g and 17.6 ± 1.77%ID/g at 4 hours and 24 hours, respectively). Although the spleen accumulations of both nanocages were comparable to those in liver at 4 hours, both significantly increased at 24-hour time point (86.9 ± 10.7%ID/g and 90.3 ± 10.9%ID/g for ^{64}Cu-AuNCs-PEG-MSH and ^{64}Cu-AuNCs-PEG, respectively, $P < .0001$ for both, n = 4/group), which was also consistent with our previous report about the size effect of nanoparticles in spleen accumulation.[25,26] Owing to the similar in vivo pharmacokinetics of the 2 nanocages, the nontargeted ^{64}Cu-AuNCs-PEG could serve as a useful control to study the tumor targeting effect enabled by the conjugation of α-MSH peptide.

Positron Emission Tomography/Computed Tomography Imaging of AuNCs-PEG-MSH

Positron emission tomography/computed tomography images of ^{64}Cu-AuNCs-PEG-MSH showed tumor accumulation at 24 hours postinjection in a B16/F10 mouse melanoma model (Figure 4A). The high uptakes in liver and spleen were also consistent with the biodistribution studies. Quantitative tumor uptake analysis demonstrated 4.57 ± 0.36%ID/g (n = 4/group) accumulation within the tumor, comparable to the results acquired with targeted gold nanospheres.[27] The nontargeted ^{64}Cu-AuNCs-PEG showed weak signals within the tumor, confirmed by the significantly lower tumor accumulation (3.40 ± 0.34%ID/g, $P < .001$, n = 4/group). Through competitive receptor blocking, the tumor accumulation of ^{64}Cu-AuNCs-PEG-MSH was significantly decreased (3.59 ± 0.30%ID/g, $P < .001$, n = 4/group), showing no statistical difference from that of ^{64}Cu-AuNCs-PEG, demonstrating the targeting specificity of ^{64}Cu-AuNCs-PEG-MSH. A further analysis of the
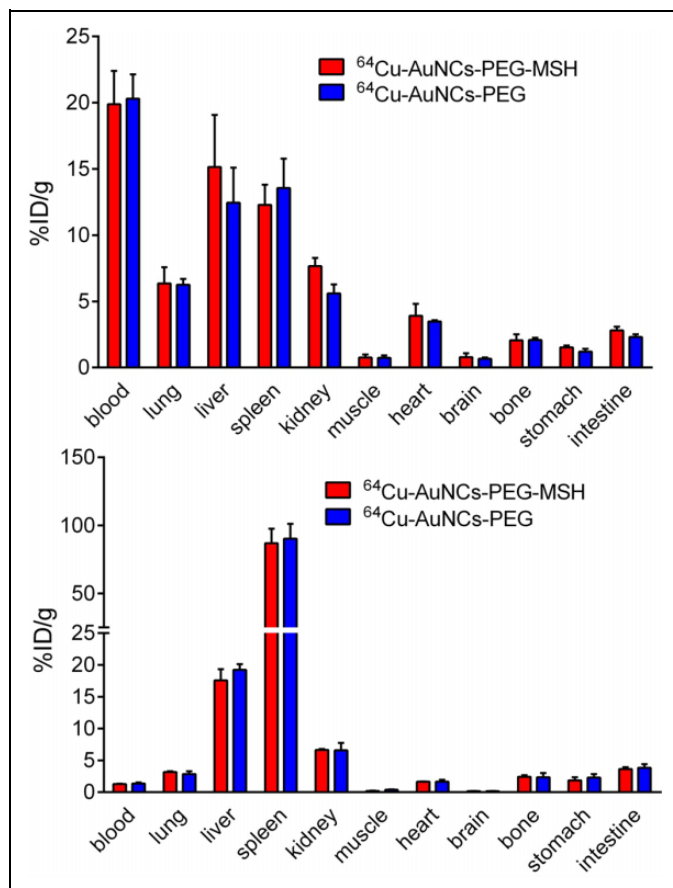
Figure 3. In vivo biodistribution of ^{64}Cu-AuNCs-PEG-MSH and ^{64}Cu-AuNCs-PEG in wild-type C57BL/6 mice at 4 (top panel) and 24 hours (bottom panel) (n = 4/group) postintravenous injection.

tumor localization showed that the tumor/muscle uptake ratio of the targeted nanocages was 20.26 $\pm$ 4.54 (n = 4/group), twice of that acquired using the nontargeted nanocages (10.11 $\pm$ 1.84, $P < .001$, n = 4/group), indicating the advantage of targeted AuNCs for cancer diagnosis.

To further improve the targeting efficiency of ^{64}Cu-AuNCs-PEG-MSH in vivo, the amount of NDP-α-MSH peptide conjugated with the surface of AuNCs was increased to 5400 copies/AuNC by increasing the molar ratio of OPPS-PEG-MSH to HS-PEG-OMe during the conjugation reaction. Interestingly, the increased conjugation of targeting NDP-α-MSH peptide also led to increased uptake in the B16/F10 tumors, as demonstrated in Figure 5A. The quantitative analysis showed the tumor localization was 7.43 $\pm$ 0.55%ID/g (n = 4/group) at 24 hours and remained stable up to 48 hours (7.52 $\pm$ 0.40%ID/g, n = 4/group). Both were twice as much as that acquired with nontargeted ^{64}Cu-AuNCs-PEG ($P < .001$, n = 4/group). Through the coinjection of nonradiolabeled AuNCs-PEG-MSH in excess amount, the tumor uptake was significantly blocked (4.58 $\pm$ 0.69%ID/g, $P < .001$, n = 4/group), suggesting the targeting specificity. Additionally, the elevated tumor uptake also led to improved tumor/muscle contrast ratio, which were 19.67 $\pm$ 0.60 at 24 hours (n = 4/group) and further

increased to 30.48 $\pm$ 1.27 at 48 hours (n = 4/group), which will help to better localize the tumor for photothermal treatment and reduce the side effect in the future. Furthermore, the improved targeting sensitivity and specificity may be particularly useful for detecting small metastatic lesions in distant organs such as liver due to the stable background hepatic accumulation during the 24-hour study.

Currently, there are a lot of effort using combined strategy for melanoma treatment such as integrating immunotherapy, BRAF inhibitor, and radiotherapy, which has shown significant efficacy in patients. However, due to the lack of noninvasive imaging approach, it is challenging to fulfill the goal of personalized therapy. The AuNCs developed herein has the potential to serve as a multivalent platform to integrate the imaging and therapy together for melanoma theranostics by loading/encapsulating small molecule inhibitors, radiolabeling with ^{67}Cu/^{64}Cu for MSH peptide-directed treatment following PET guidance.[28-31]

Characterization of MC1R Receptor

Histopathological analysis of B16/F10 tumor and characterization of MC1R receptor was also performed in the collected tumor tissues. As shown in Figure 6, the hematoxylin and eosin staining showed a high level of large and polynucleated tumor cells in the B16/F10 tumors collected at 10 days postimplant. Immunohistochemical staining of the tumor demonstrated the high expression of MC1R receptor in malignant melanocytes across the tumor (Figure 6), which is consistent with high targeting effect of ^{64}Cu-AuNCs-PEG-MSH.

Conclusion

In summary, we have demonstrated the synthesis of MSH-conjugated AuNCs with well-defined structure and surface chemistry for MC1R-targeted imaging in a mouse B16/F10 melanoma model. The high radiolabeling-specific activity of AuNCs ensured the trace amount administration for in vivo applications. Pharmacokinetic evaluation of ^{64}Cu-AuNCs-PEG-MSH showed high initial blood circulation, followed by fast clearance for low background. Positron emission tomography/computed tomography imaging of the MC1R-targeted ^{64}Cu-AuNCs-PEG-MSH demonstrated sensitive and specific detection of MC1R in the B16/F10 tumors, confirmed by the overexpression of MC1R in tumor cells. By increasing the loading of targeting α-MSH peptide onto the surface of AuNCs, the tumor targeting efficiency was also increased, indicating the effectiveness of this targeting strategy in improving tumor delivery for potential photothermal therapy. However, there are also some limitations associated with the current studies. The biodistribution profile of ^{64}Cu-AuNCs-PEG-MSH needs to be improved to reduce MPS system accumulation and minimize any potential toxicity concerns. The targeting efficiency needs to be further enhanced for future photothermal treatment studies.
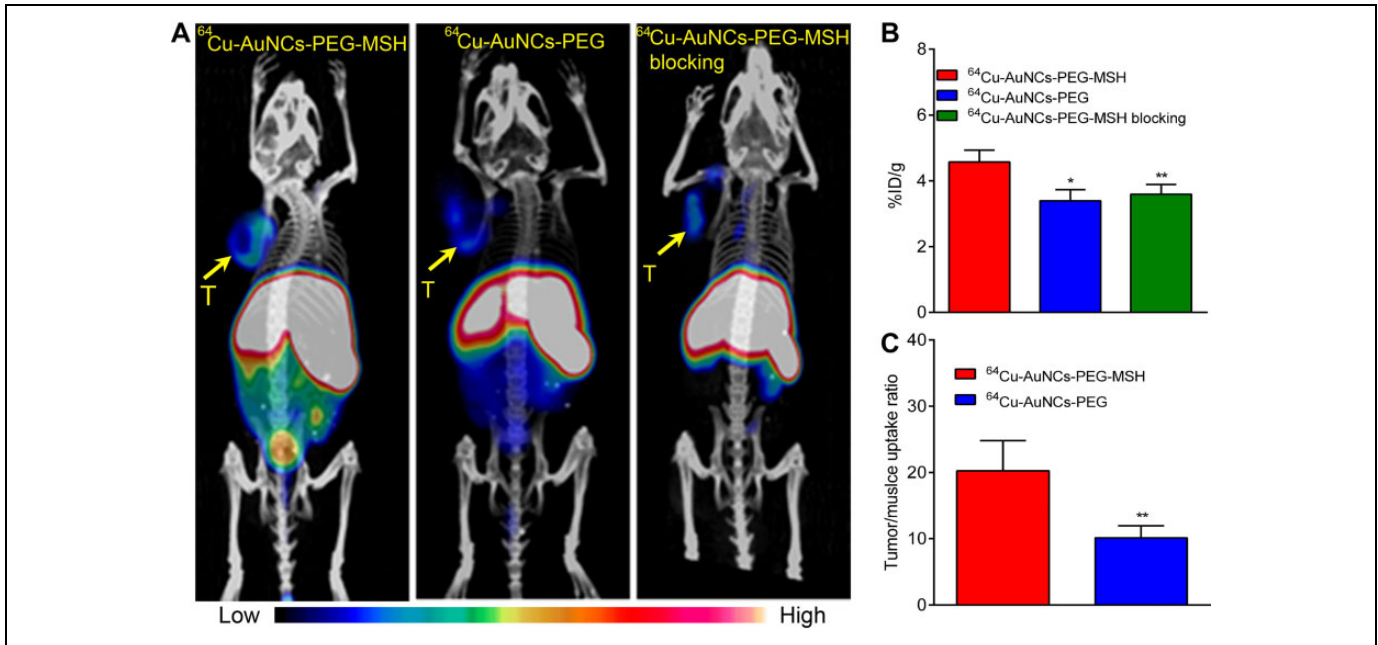
Figure 4. A, Representative positron emission tomography/computed tomography (PET/CT) images of ^{64}Cu-AuNCs-PEG-MSH, ^{64}Cu-AuNCs-PEG, and competitive receptor blocking in mice bearing B16/F10 melanoma at 24 hours postinjection. The blocking study was carried by coinjection of nonradiolabeled AuNCs-PEG-MSH in excess (molar ratio of AuNCs-PEG-MSH to ^{64}Cu-AuNCs-PEG-MSH at 40:1; yellow Arrow T, Tumor). B, Quantitative tumor uptakes of ^{64}Cu-AuNCs-PEG-MSH, ^{64}Cu-AuNCs-PEG, and blocking studies at 24 hours. (n = 4/group). C, Tumor-to-muscle ratio of ^{64}Cu-AuNCs-PEG-MSH and ^{64}Cu-AuNCs-PEG at 24 hours (n = 4 / group). *P < .05, **P < .001.
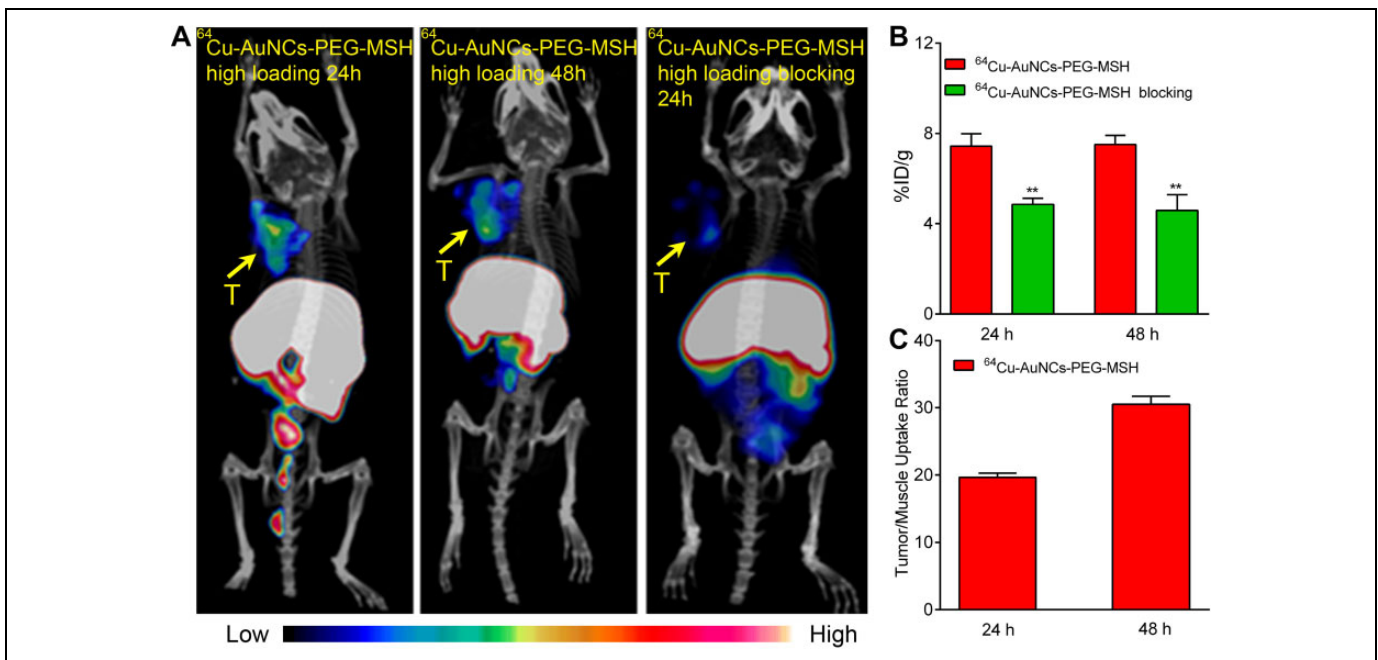
Figure 5. A, Representative positron emission tomography/computed tomography (PET/CT) images of ^{64}Cu-AuNCs-PEG-MSH with high loading of α-melanocyte-stimulating hormone (α-MSH) peptide and competitive receptor blocking studies in mice-bearing B16/F10 melanoma at 24 and 48 hours postinjection. The competitive blocking studies were carried with coinjection of non-radiolabeled AuNCs-PEG-MSH conjugated with a high loading of α-MSH peptide in excess amount (molar ratio of AuNCs-PEG-MSH: ^{64}Cu-AuNCs-PEG-MSH = 40:1; T, tumor). B, Quantitative tumor uptake analysis at 24 and 48 hours (n = 4/group). C, Tumor-to-muscle ratio of ^{64}Cu-AuNCs-PEG-MSH with high α-MSH peptide at 24 and 48 hours (n = 4/group). *P < .005, **P < .001.
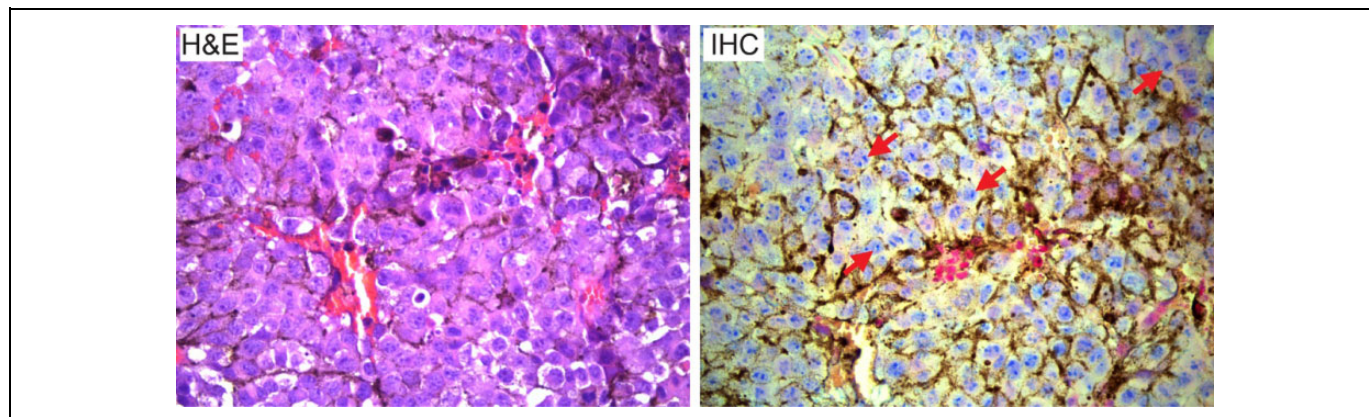
Figure 6. Hematoxylin and eosin (H&E) staining of B16/F10 tumor tissue showing large and polynucleated tumor cells. Immunohistochemical staining of MC1R receptor in B16/F10 tumor. Tumor cells are stained with MC1R (blue) and counterstained with nuclear fast red (pink). The brown color indicates melanin expression (marked by arrows). All panels are at ×400.

Author's Note

Yongfeng Zhao and Bo Pang contributed equally to this work.

Declaration of Conflicting Interests

Funding

ORCID iD

Yongjian Liu 🔟 http://orcid.org/0000-0002-1118-1535

References

1. Siegel RL, Miller KD, Jemal A. Cancer statistics, 2017. *CA: Cancer J Clin*. 2017;67(1):7–30.

2. Giljohann DA, Seferos DS, Daniel WL, Massich MD, Patel PC, Mirkin CA. Gold nanoparticles for biology and medicine. *Angew Chem Int Ed*. 2010;49(19):3280–3294.

3. Garbe C, Eigentler TK, Keilholz U, Hauschild A, Kirkwood JM. Systematic review of medical treatment in melanoma: current status and future prospects. *Oncologist*. 2011;16(1):5–24.

4. Berciano-Guerrero MA, Montesa-Pino A, Castaneda-Penalvo G, Munoz-Fernandez L, Rodriguez-Flores J. Nanoparticles in melanoma. *Curr Med Chem*. 2014;21(32):3701–3716.

5. You S, Luo J, Grossniklaus HE, Gou ML, Meng K, Zhang Q. Nanomedicine in the application of uveal melanoma. *Int J Ophthalmol*. 2016;9(8):1215–1225.

6. Iyer AK, Khaled G, Fang J, Maeda H. Exploiting the enhanced permeability and retention effect for tumor targeting. *Drug Discov Today*. 2006;11(17-18):812–818.

7. Hu M, Chen J, Li Z-Y, et al. Gold nanostructures: engineering their plasmonic properties for biomedical applications. *Chem Soc Rev*. 2006;35(11):1084–1094.

8. Pissuwan D, Valenzuela SM, Cortie MB. Therapeutic possibilities of plasmonically heated gold nanoparticles. *Trends Biotechnol*. 2006;24(2):62–67.

9. Bhise K, Sau S, Alsaab H, Kashaw SK, Tekade RK, Iyer AK. Nanomedicine for cancer diagnosis and therapy: advancement, success and structure-activity relationship. *Ther Deliv*. 2017; 8(11):1003–1018.

10. Pang B, Zhao Y, Luehmann H, et al. 64Cu-Doped PdCu@Au Tripods: a multifunctional nanomaterial for positron emission tomography and image-guided photothermal cancer treatment. *ACS Nano*. 2016;10(3):3121–3131.

11. Deng H, Zhong Y, Du M, et al. Theranostic self-assembly structure of gold nanoparticles for NIR photothermal therapy and X-Ray computed tomography imaging. *Theranostics*. 2014;4(9): 904–918.

12. Wang Y, Black KCL, Luehmann H, et al. A comparison study of gold nanohexapods, nanorods, and nanocages for photothermal cancer treatment. *ACS Nano*. 2013;7(3):2068–2077.

13. Wang Y, Liu Y, Luehmann H, et al. Evaluating the pharmacokinetics and in vivo cancer targeting capability of au nanocages by positron emission tomography imaging. *ACS Nano*. 2012;6(7): 5880–5888.

14. Wang Y, Liu Y, Luehmann H, et al. Radioluminescent gold nanocages with controlled radioactivity for real-time in vivo imaging. *Nano Lett*. 2013;13(2):581–585.

15. Black KCL, Wang Y, Luehmann HP, et al. Radioactive 198Au-doped nanostructures with different shapes for in vivo analyses of their biodistribution, tumor uptake, and intratumoral distribution. *ACS Nano*. 2014;8(5):4385–4394.

16. Moon GD, Choi S-W, Cai X, et al. A new theranostic system based on gold nanocages and phase-change materials with unique features for photoacoustic imaging and controlled release. *J Am Chem Soc*. 2011;133(13):4762–4765.

17. Rosenkranz AA, Slastnikova TA, Durymanov MO, Sobolev AS. Malignant melanoma and melanocortin 1 receptor. *Biochemistry (Mosc)*. 2013;78(11):1228–1237.

18. Miao Y, Benwell K, Quinn TP. 99mTc- and 111In-labeled α-Melanocyte-stimulating hormone peptides as imaging probes

for primary and pulmonary metastatic melanoma detection. *J Nucl Med*. 2007;48(1):73–80.

19. Lu W, Xiong C, Zhang G, et al. Targeted photothermal ablation of murine melanomas with melanocyte-stimulating hormone analog–conjugated hollow gold nanospheres. *Clin Cancer Res*. 2009;15(3):876–886.

20. Kim C, Cho EC, Chen J, et al. In vivo molecular photoacoustic tomography of melanomas targeted by bioconjugated gold nanocages. *ACS Nano*. 2010;4(8):4559–4564.

21. Skrabalak SE, Au L, Li X, Xia Y. Facile synthesis of Ag nanocubes and Au nanocages. *Nat Protoc*. 2007;2(9):2182–2190.

22. Liu Y, Ibricevic A, Cohen JA, et al. Impact of hydrogel nanoparticle size and functionalization on in vivo behavior for lung imaging and therapeutics. *Mol Pharm*. 2009;6(6):1891–1902.

23. Choi HS, Liu W, Misra P, et al. Renal clearance of quantum dots. *Nat Biotechnol*. 2007;25(10):1165–1170.

24. Lipka J, Semmler-Behnke M, Sperling RA, et al. Biodistribution of PEG-modified gold nanoparticles following intratracheal instillation and intravenous injection. *Biomaterials*. 2010; 31(25):6574–6581.

25. Jørgensen JT, Persson M, Madsen J, Kjær A. High tumor uptake of 64Cu: implications for molecular imaging of tumor characteristics with copper-based PET tracers. *Nucl Med Biol*. 2013;40(3):345–350.

26. Zhao Y, Sultan D, Detering L, et al. Copper-64-alloyed gold nanoparticles for cancer imaging: improved radiolabel stability and diagnostic accuracy. *Angew Chem Int Ed Engl*. 2014;53(1):156–159.

27. Lu W, Xiong C, Zhang R, et al. Receptor-mediated transcytosis: a mechanism for active extravascular transport of nanoparticles in solid tumors. *J Control Release*. 2012;161(3):959–966.

28. Novak-Hofer I, Schubiger PA. Copper-67 as a therapeutic nuclide for radioimmunotherapy. *Eur J Nucl Med Mol Imaging*. 2002; 29(6):821–830.

29. Stokes WA, Binder DC, Jones BL, et al. Impact of immunotherapy among patients with melanoma brain metastases managed with radiotherapy. *J Neuroimmunol*. 2017;313:118–122.

30. Geukes Foppen MH, Boogerd W, Blank CU, van Thienen JV, Haanen JB, Brandsma D. Clinical and radiological response of BRAF inhibition and MEK inhibition in patients with brain metastases from BRAF-mutated melanoma. *Melanoma Res*. 2018;28(2):126–133.

31. Hecht M, Meier F, Zimmer L, et al. Clinical outcome of concomitant vs interrupted BRAF inhibitor therapy during radiotherapy in melanoma patients. *Br J Cancer*. 2018;118(6):785–792.